Chinese Chemical Letters 34 (2023) 107229

Contents lists available at ScienceDirect

Chinese Chemical Letters

journal homepage: www.elsevier.com/locate/cclet

TiO_2-carbon porous nanostructures for immobilization and conversion of polysulfides

Keke Gao[a,1], Rui Xu[a,1], Yunxiang Chen[a], Zongtao Zhang[a,*], Jiashuo Shao[a], Haipeng Ji[a], Liying Zhang[a], Shasha Yi[a], Deliang Chen[a], Junhua Hu[a], Yanfeng Gao[a,b]

[a] *School of Materials Science and Engineering, Zhengzhou University, Zhengzhou 450001, China*
[b] *School of Materials Science and Engineering, Shanghai University, Shanghai 200444, China*

ARTICLE INFO

Article history:
Received 9 December 2021
Revised 13 January 2022
Accepted 15 February 2022
Available online 19 February 2022

Keywords:
Hierarchical porous carbon
Phase separation
MXene
Interlayer
Lithium-sulfur battery

ABSTRACT

Lithium-sulfur batteries (LSBs) are among the most promising series of next-generation high density energy storage systems. However, the problem of “shuttle effect” caused by dissolution and migration of polysulfide intermediates has severely inhibited their practical applications. Herein, TiO_2-carbon nanocomposites embedded hierarchical porous carbon (T-*h*PC) interlayers are fabricated *via* Ti_3C_2 MXene assisted phase separation and annealing method. The T-*h*PC processes micro- to macro-scale multi-pores along with highly adsorptive and catalytic carbon supported TiO_2 nanoparticles, which significantly enhances the polysulfides immobilization and improves the redox reaction kinetics when applied as lithium-sulfur battery interlayers. An initial discharge specific capacity of 1551.1 mAh/g and a stable capacity of 893.8 mAh/g after 200 cycles at 0.5 C are obtained, corresponding to a capacity decay rate of only 0.04% per cycle. The investigations in this paper can provide a simple and effective strategy to enhance the electrochemical properties for lithium-sulfur batteries.

With the rapid growth of portable electronic devices and electric vehicles, the requirements of batteries with high energy density and long-lasting performances are becoming more and more urgent. Currently, commercial lithium-ion batteries (LIBs) almost approach their energy density limits [1,2]. Comparatively, the theoretical energy density for lithium-sulfur batteries (LSBs) is 4–5 times as much as that of LIBs, which is now attracting extensive attentions in both fundamental research and industrial application [3]. Furthermore, sulfur is non-toxic and abundant in nature, which endows it an environment-friendly energy material with low cost [4]. However, the commercialization of LSBs is severely hampered by several issues, including the poor conductivity of sulfur, the large volume expansion during charging and discharging, and the shuttle effect of polysulfides (PSs) [5,6]. Among these, the dissolution of polysulfide intermediates into the organic electrolyte and their subsequent migrations between the cathode and the anode cause serious loss of the active material and the decrease of Coulombic efficiency [7,8].

In view of the polysulfides shuttling, physical confinements are the most commonly adopted strategies, by compositing active sulfur with porous carbon materials possessing various kinds of holes or caves [9,10]. However, due to the non-polar nature of carbon materials, only weak interactions with the polar polysulfides can be introduced, limiting their efficiency to trap the polysulfides [11]. Therefore, a variety of polar materials, such as hetero-atom doped carbon materials [12,13], single atoms [14], TiO_2 [15], Co_3Se_4 [16], Ti_3C_2 [17], are explored to further enhance their interactions with the polysulfides. Significantly reduced shuttle effect and improved cycling performance are demonstrated for these cells [18], although, in most cases, a reduction in the total energy density is also accompanied due to the uptake of extra spaces by these hosts [19]. Electrolyte, another essential component that can function as “bridge” for cathode and anode and handle the important task of lithium ions transportation, also shows important progresses these years on PSs regulation. As indicated by Nazar [6] and Zhang [8], by careful composition design, modified electrolyte can regulate the redox reaction kinetics and improve the stability of Li metal anodes in Li-S batteries. However, the diversity of electrolyte and perplexing side effects during reaction makes it quite challenging to explorer the underlying modification system.

Interlayer is another frequently reported architecture to obstruct the polysulfides, which can be feasibly inserted between the cathode and the separator [20]. Various carbon-based materials, such as carbon nanotubes [21], graphene [22] and porous car-

---

[*] Corresponding author.
E-mail address: ztzhang@zzu.edu.cn (Z. Zhang).
[1] These authors contributed equally to this work.

https://doi.org/10.1016/j.cclet.2022.02.034
1001-8417/© 2022 Published by Elsevier B.V. on behalf of Chinese Chemical Society and Institute of Materia Medica, Chinese Academy of Medical Sciences.

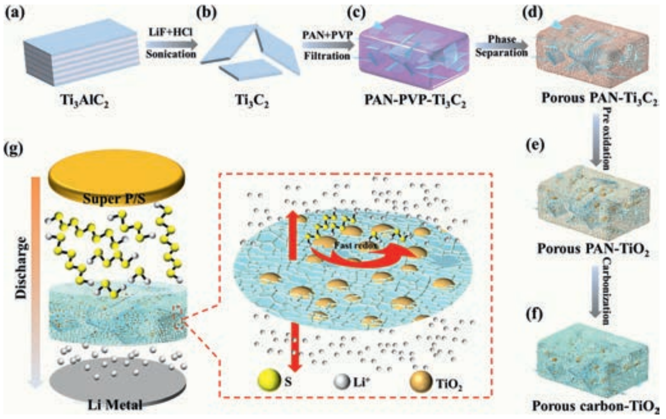

Fig. 1. (a-f) Schematic illustration for the synthesis of the hierarchical porous carbon interlayer embedded with nano TiO$_2$. (g) Schematic of cell configuration with a T-*h*PC interlayer and demonstration of the 3D hierarchical porous T-*h*PC interlayer for polysulfides stabilization and Li$^+$ transportation.

bon [23,24], are successfully incorporated as the interlayers, due to their excellent conductivity, abundant porous structure and easily adjustable morphology. However, the effectiveness of carbon-based interlayers to inhibit the polysulfides shuttling is still limited, because of the weak interaction with the polar polysulfides. Progressively, a variety of polar materials, such as Ti$_3$C$_2$ MXene [25,26], MoS$_2$ [27] and V$_2$O$_5$ [28], are applied by introducing chemical interactions to trap the polysulfides and improve the Coulombic efficiency. Among these, the two-dimensional (2D) conductive materials of MXene, which have large specific surface areas and bountiful chemical functional groups [29], have attracted special research attentions as lithium-sulfur battery interlayers. For example, Wu *et al.* [30] report an all-MXene-based flexible Li-S battery by utilizing alkalized Ti$_3$C$_2$ MXene nanoribbons as the sulfur host and delaminated Ti$_3$C$_2$ MXene nanosheets as the interlayer. Strong chemical absorption and physical blockings are demonstrated, accompanied with an effective prevention over the shuttle of lithium polysulfides. Also, by in situ solution oxidation, TiO$_2$-MXene heterostructures is synthesized from the Ti$_3$C$_2$ colloidal solutions [31], and improved polysulfides diffusion between the TiO$_2$-MXene hetero-interfaces and enhanced catalytic activity due to the oxygen-terminated MXene surface are endowed. Moreover, many other benefits on polysulfides regulation and the electrochemical enhancement can also be expected from the MXene, ascribed to their catalytic functions with manipulable chemical components and tailored surface chemistry [32–34]. However, it should be noticed that continuous captures of the polysulfides by 2D polar additives also leads to the loss of active surface and the blocking of lithium ion (Li$^+$) transport channels, resulting in a decline in the electrochemical performance [35,36]. Effective steps to combine the polysulfides inhabitation and Li$^+$ transportation is urgently needed for high performance Li-S batteries.

Building hierarchical porous conductive skeleton structures is an important choice that is tendentiously applied to balance the Li$^+$ transportation and the LiPSs stabilization, by introducing multilevel pore structures with micropores (<2 nm), mesopores (2–50 nm) and/or macropores (>50 nm) to provide complementary ion channels and confined spaces for LiPSs storage [37]. For example, Wang *et al.* [38] report nitrogen and sulfur co-doped hierarchical porous carbon (NSHPC) by carbonization of lotus seedpod shells, which remarkably reduces the charge transfer impedance and enhances the chemisorption ability for polysulfides. Recently, by using the linear-polyethylenimine (L-PEI) as template, we have elaborately synthesized 3D hierarchical porous carbon nanonet flakes (CNNFs) decorated with MoS$_2$ nanosheets that show enhanced adsorptive and catalytic bifunctionalities, where LSBs with high energy density and ultra-high stability are obtained [39]. It is worth taking steps to construct hierarchical carbon structures for high performance lithium-sulfur batteries.

Phase separation method has been widely reported as effective means to prepare multi-scale porous structures [40]. The solvent/non-solvent induced phase separation in polymer solutions can produce polymer-rich and solvent-rich domains, where the former ones can form carbon-containing frames after carbonization and the latter can produce pores in different ranges [41]. By regulation of the polymer type, the solvent, and the temperature for phase separation, various kinds of porous structures could be generated [41–43]. In addition, the pore size and its distribution can further be modified, by introducing additional pore-forming agent during the phase separation, *e.g.*, commercially available polyvinyl pyrrolidone (PVP), which is soluble both in the deionized water (the nonsolvent) and the matrix polymer and can feasibly induce additional pores in micro- to meso-scale ranges in the blend matrix by dissolution in water [44]. The simple and large-scale pore-structure modulable advantages endow the phase separation method a great potential for the synthesis of hierarchical porous carbon materials applicable in energy fields.

To fulfill the benefits of 2D MXene and their derivates with modulable functionality and the hierarchical porous carbon structures with complementary electron/ion pathways, phase separation and subsequent annealing method are applied to construct a novel TiO$_2$-carbon nanocomposite embedded hierarchical porous carbon (T-*h*PC). PAN and PVP are used as the main carbon source and the pore-forming agent, respectively. The MXene-derived lamellar-like TiO$_2$-carbon composites enhance the polysulfides immobilization and catalytic bifunctions. Moreover, the space confinements and the reduced transport resistance of Li$^+$ from the hierarchical porous structure significantly improve the electrochemical stability of the lithium-sulfur battery. An initial specific capacity of 1551.1 mAh/g and a discharge specific capacity of 893.8 mAh/g after 200 cycles at 0.5 C are obtained, corresponding to a capacity decay rate of 0.04% per cycle, which enlists the current processing a quite competitive strategy for high-performance lithium-sulfur batteries.

As a unique approach to fabricate hierarchical porous materials, we have established a modified phase separation method by using Ti$_3$C$_2$ MXene as the template to construct the TiO$_2$-carbon composite. The synthetic route of the T-*h*PC is schematically illustrated in Fig. 1. As shown in Fig. 1, Ti$_3$C$_2$ nanosheets are directly obtained by delamination of Ti$_3$AlC$_2$ powders, in hydrochloric acid and lithium fluoride solution [45], which are further mixed with PAN and PVP blends in DMF solvent. Subsequently, highly porous PAN skeletons with MXene sheets are formed by a water induced phase separation, where the DMF-soluble PAN rapidly precipitates and shrinks to form abundant large pores after contact with the nonsolvent of water. As PVP is soluble both in DMF and water, additional pores with much smaller sizes (nano- to meso-scale) can also be formed in the PAN-dominant matrix after dissolution in water. Furthermore, a pre-oxidation process at around 180 °C for 12 h is performed to avoid the unfavorable melt and pore-structure collapse of the PAN polymers during the sequent carbonization, where Ti$_3$C$_2$ MXene are also oxidized into TiO$_2$-carbon composites.

The structure of the as-obtained Ti$_3$C$_2$ MXene is investigated by X-ray diffraction (XRD) (Fig. S1 in Supporting information). The characteristic (104) diffraction peak for Ti$_3$AlC$_2$ disappears after chemical etching applied, indicating the successful delamination of Al-atom layer from Ti$_3$AlC$_2$ precursor [46]. Also, the diffraction peak at low angle shifts significantly from 9.6° to 5.9°, confirming the increase of interplanar distance for the Ti$_3$C$_2$ MXene (002) lattice plane [47]. Field-emission scanning electron microscopy (FE-SEM) (Fig. 2a), further shows the typical 2D lamellar structures

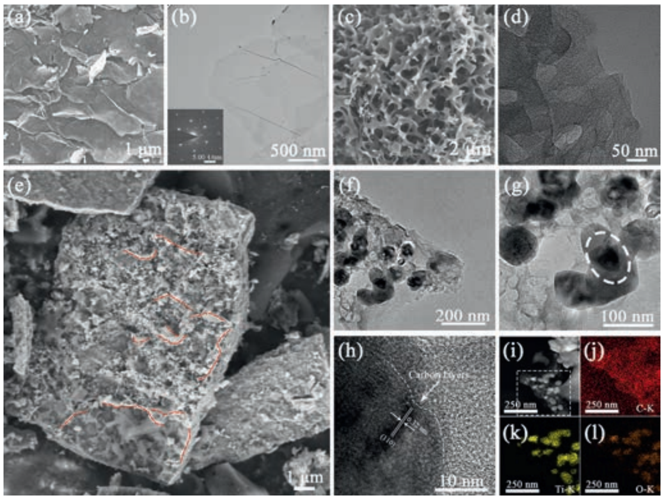

Fig. 2. (a) SEM and (b) TEM image of the Ti_3C_2 MXene. The inset in the TEM shows the SAED pattern. (c) SEM and (d) TEM image of *h*PC. (e) SEM and (f-h) TEM images for T-*h*PC. The composition marked in red in (e) shows some of the lamellar-structured TiO_2-carbon composites in the samples. (i) The STEM dark field images and the corresponding EDX elemental mappings of (j) C, (k) Ti and (l) O, respectively, for the T-*h*PC.

for the MXene phases with lateral sizes of about 1~2 μm, and no distinct wrinkles or stackings can be found, indicating the high quality of the delaminated Ti_3C_2 MXene [48,49]. Transmission electron microscopy (TEM) and selected area-electron diffraction (SAED) (Fig. 2b), further demonstrates a typical hexagonal symmetric structure with single or few-layered crystalline Ti_3C_2 [50]. Furthermore, the morphology and the pore structure of the porous carbon obtained by phase separation and the subsequent carbonization are also investigated by SEM and TEM (Figs. 2c and d, Fig. S3 in Supporting information). It can be seen that pure PAN-derived carbon (PC) shows distinct finger-like pores with a large pore volume [50]. In contrast, after introduction of PVP molecular, spongy-like structures with much more smaller interpenetrating pores are produced [51,52]. Specifically, the water-soluble PVP can migrate into the aqueous phase after fast solvent exchange during the phase separation [44], where additional pores with rough surfaces can be formed in the PAN matrix.

The addition of Ti_3C_2 MXene can influence the structures of the porous carbon drastically. As shown in the SEM image (Fig. 2e), a denser packing of the porous carbon embedded with distinct layer-structured compositions compared with the PC and the *h*PC can be found. TEM and high-resolution TEM (HRTEM) images (Figs. 2f-h), further indicate that these layered aggregates are composed of tens of nanometers TiO_2 nanoparticles and thin porous carbon materials. Lattice fringes with lattice spacing of 0.32 nm can be found clearly which is assigned to the typical (110) lattice plane for rutile TiO_2 (R-TiO_2), and the close contact between TiO_2 and the thin carbon layer can also be clearly observed. The formation of R-TiO_2 is consistent with the XRD results in following sections, which indicates that Ti_3C_2 are oxidized into R-TiO_2 after hydrothermal and carbonization [53]. Energy dispersive spectroscopy (EDS) mappings (Figs. 2i-l), show that the Ti and O atoms are mainly distributed along the TiO_2 nanoparticles in the T-*h*PC. The formation of layer-structured TiO_2-carbon composites is expected to enhance the electrochemical performance for Li-S batteries, where beneficial adsorptive and catalytic sites for the LiPSs can be introduced [54].

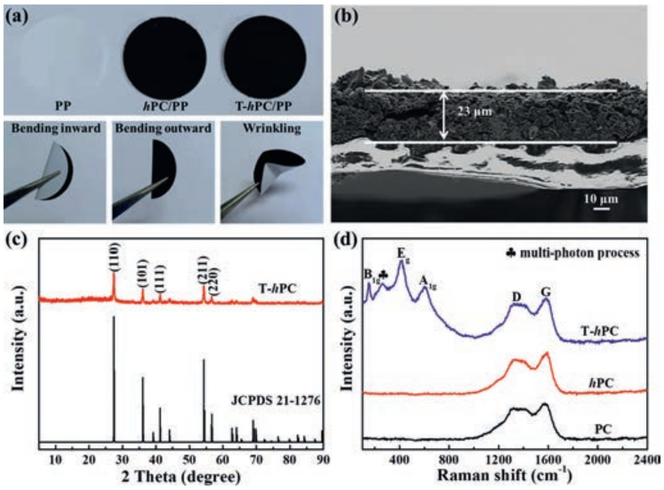

Fig. 3. (a) Photographs of the PP, *h*PC/PP and T-*h*PC/PP separators and the T-*h*PC/PP separators under various mechanical tests. (b) Cross-sectional SEM images for the T-*h*PC/PP. (c) XRD patterns of the T-*h*PC. Standard diffraction pattern for rutile TiO_2 (JCPDS No. 21-1276) is also shown. (d) Raman spectra of the PC, *h*PC and T-*h*PC, respectively.

Fig. 3a and Fig. S4 (Supporting information) show the photographs of the PP, *h*PC/PP and T-*h*PC/PP separators. A smooth and uniform surface configuration can be seen for the T-*h*PC, which can also display excellent mechanical stability that can withstand the stresses induced by bending and wrinkling. The SEM cross-section image of the T-*h*PC/PP indicates a smooth thin layer with 23 μm-thick coating for the interlayer (Fig. 3b). Compared the routine PP separator with defined stretched holes, a hierarchical porous structure is found for the T-*h*PC modified separators, which is beneficial for electrolyte storage and permeation (Figs. S4a-c in Supporting information). Notably, the wettability of the *h*PC/PP and T-*h*PC/PP are improved significantly, with a decreased electrolyte contact angle from 20° (for PP) to nearly 0° (for *h*PC/PP and T-*h*PC/PP) (Figs. S4d-f in Supporting information). The enhanced wettability is expected to provide fast ion transportation during the electrochemical redox processes [55].

To investigate the structure and compositions of the T-*h*PC, XRD and Raman analyses are further performed, which are shown in Fig. 3. After phase separation and subsequent carbonization, the characteristic peak of MXene (002) crystal planes completely disappeared, and additional diffraction peaks centered at 27° and 36° can be observed, corresponding to the (110) and (101) crystal planes of the rutile TiO_2 (R-TiO_2) [56], respectively (Fig. 3c). Raman spectra (Fig. 3d) for all samples show the typical D and G bands for carbon locating at 1338 cm^{-1} and 1583 cm^{-1}, respectively, corresponding to the sp^3 hybridization and in plane defects of the graphitic carbon [57], respectively. Furthermore, the ratio (0.96) of I_D/I_G is less than 1, indicating a high degree of graphitization after carbonization [58], which is conducive for electron/ion conductivity [12,59]. Raman modes for MXene, centered at 201, 380 and 645 cm^{-1} [60], have not been detected in the T-*h*PC, although additional Raman modes centered at 149, 260, 414 and 607 cm^{-1} are found, which can be assigned to the B_{1g}, multi-photon process, E_g and A_{1g} vibrations for R-TiO_2 [61,62]. The above results further verify that the components of Ti_3C_2 are oxidized into R-TiO_2 for the T-*h*PC.

The chemical state and surface compositions of the T-*h*PC are further analyzed by X-ray photoelectron spectroscopy (XPS) (Fig. 4a). XPS survey spectrum indicates the existence of carbon, oxygen, titanium, and nitrogen signals in the sample. High-resolution XPS spectrum (Fig. 4b) for C 1s can be divided into three individual bonds, that is, C–C (284.6 eV), C–N (285.3 eV) and O–C=O (288.7 eV), respectively [63]. The existence of C–N bond can be attributed to pyrolysis of PAN molecules containing nitrogen functional group (C≡N) [64]. Notably, the Ti–C bond in Ti_3C_2 MXene,

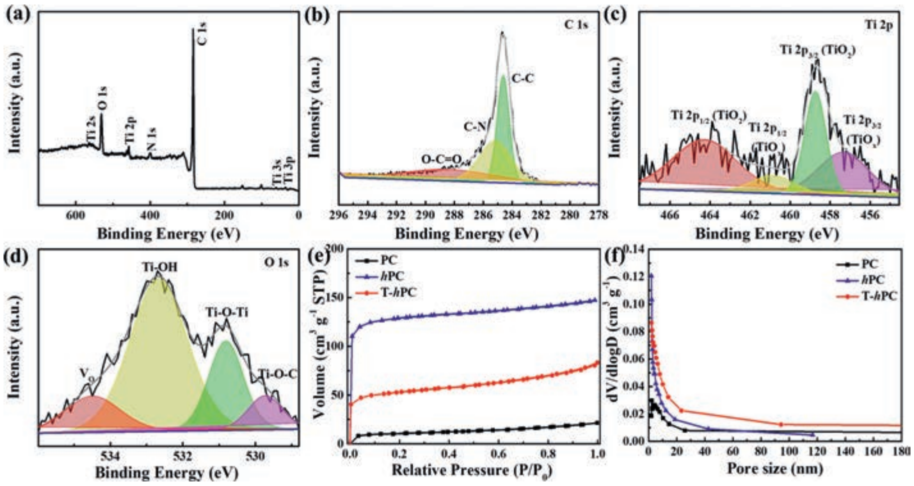

Fig. 4. (a) XPS survey spectrum and high-resolution spectra of (b) C 1s, (c) Ti 2p and (d) O 1s for the T-*h*PC. (e, f) The nitrogen adsorption/desorption isotherms and the pore-size distribution curves for the PC, *h*PC and T-*h*PC, respectively.

with binding energy of 281.7 eV, has not been detected, illustrating the successful removal of the Ti−C bond after pro-oxidization and carbonization [65,66]. For the Ti signal, two distinct peaks centered at 458.7 eV and 464.3 eV, respectively, can be found in the fitted high-resolution spectra of Ti 2p (Fig. 4c), which can be assigned to the Ti $2p_{3/2}$ (Ti−O) and Ti $2p_{1/2}$ (Ti−O) in typical TiO_2 crystals [67]. Meanwhile, two other fitted peaks centered at 457.4 eV and 461.1 eV, respectively, can be observed, which are usually ascribed to the oxygen-deficient defects in TiO_2 [68,69], namely, Ti $2p_{3/2}$ (TiO_{2-x}) and Ti $2p_{1/2}$ (TiO_{2-x}). It is reported that the presence of anion defects is beneficial for the electrochemical reactions in a Li-S battery, by introducing active sites and stronger V_o−S bond between the S atom in polysulfides and the surface oxygen vacancy in TiO_{2-x} [70,71]. The formation of oxygen-deficient TiO_{2-x} is also confirmed by the high resolution spectrum of O 1s (Fig. 4d), where a distinct binding energy centered at 534.8 eV assigning to V_o [72,73], can be found. Besides, the other two peaks centered at 530.8 eV and 532.6 eV, respectively, are attributed to Ti−O−Ti and Ti−OH in TiO_2 [70,74]. Impressively, the peak centered at 529.7 eV in the high-resolution O 1s spectrum, are expected to be the Ti−O−C bond formed between the *h*PC and TiO_2 interfaces [75]. It is reported that the formation of Ti–O–C bond can provide a conductive pathway for charge carriers between TiO_2 and T-*h*PC matrix, resulting in decreased charge transfer resistance [76–78]. For the N 1s spectrum, four fitted peaks centered at 398.1 eV, 399.4 eV, 400.7 eV and 402.3 eV, respectively, can be found (Fig. S5 in Supporting information), which can be assigned to pyridinic N, pyrrolic N, graphitic N and oxidized N [55]. Due to the strong electronegativity of nitrogen, N-doped carbon materials can prompt the chemisorption of lithium polysulfides through the Li-N interactions and enhance their electroconductivity [23].

Nitrogen adsorption-desorption isotherms are further performed to investigate the pore structures for the samples, as shown in Figs. 4e and f. Compared with PC, the sample of *h*PC exhibits a sharp increase in nitrogen adsorption at a relative low pressure ($0.00 < P/P_0 < 0.05$), showing a typical I type isotherm, which is an indicative of the presence of the abundant micropores [79]. However, after the introduction of PVP pore-forming agent, micro/meso-porous structures are found in the sample (*h*PC). The calculated specific surface areas for PC and *h*PC are 35.2 m^2/g and 394.3 m^2/g, corresponding to the average pore sizes of 5.2 nm and 4.0 nm, respectively. Summary of the detailed pore parameters for the PC and *h*PC is present in Table S1. Obviously, the introduction of PVP significantly increases the contents of micropores in the whole system. For the T-*h*PC, a typical IV type adsorption isotherm can be found, in which a small hysteresis with the specific surface area of 164.9 m^2/g can be observed in the P/P_0 range of $0.45 < P/P_0 < 0.9$, indicating the coexistence of micro- and meso-pores in the sample [80]. The differences in the pore structure between the *h*PC and the T-*h*PC may derive from the fact that MXene, as a template, can inhibit the aggregation of the PAN polymers during phase separation and carbonization, similar results of which are also reported in ref [81].

To show the strong interaction of the T-*h*PC toward polysulfides, adsorption experiments are performed by soaking the same amounts of interlayer materials in Li_2S_6 solution (Fig. 5a). A rapid discoloration for the T-*h*PC can be found, whereas the *h*PC-containing Li_2S_6 solution still maintains light yellow color after keeping for 5 h, indicating the T-*h*PC is highly adsorptive to the polysulfides species. Moreover, to confirm the electrocatalytic effect of the T-*h*PC on LiPS conversions, symmetric cells with and without 0.4 mol/L Li_2S_6 electrolyte are assembled and tested with CV at a scan rate of 0.5 mV/s between −1.0 V to 1.0 V (Fig. 5b). Obviously, the cell with the Li_2S_6 addition shows distinct redox peaks, indicating that T-*h*PC is preferring to catalyzing conversion for LiPSs [82]. Electrochemical impedance spectra (EIS) (Fig. 5c) are also tested on these symmetric cells, which show a smaller semicircle, corresponding to a smaller charge transfer resistance (R_{ct}), for the T-*h*PC, indicating that a more efficient charge transfer occurs between the T-*h*PC and the electrolyte interfaces. Meanwhile, the corresponding equivalent circuit is present in the inset, where the intercepts of the real axis and the semicircle diameter in the high-frequency region stand for the intrinsic electrolyte resistance (R_e) of the cell and R_{ct} at the electrode/electrolyte interfaces, respectively. Meanwhile, the sloping line in the low-frequency region represents the Warburg impedance (W_o), which is related to Li-ion diffusion in electrode. Also, a constant phase element (CPE) is introduced in the simulation [83]. Based on the fitted equivalent electrical circuit model, the T-*h*PC symmetrical cell displays a smaller semicircle (1.2 Ω) than that of the *h*PC (260 Ω), revealing improved charge transfer for the polysulfides at T-*h*PC/electrolyte interface. Tafel plots are also applied to test the electrocatalytic effect for different samples, which is an effective indicator for the kinetics of sulfur redox reactions (Fig. 5d). The T-*h*PC/PP cell shows the lowest Tafel slope of 26 mV/dec for the Li_2S_n to Li_2S among the three cells 38 mV/dec for *h*PC/PP and 103 mV/dec for PP, respectively, indicating an accelerated kinetics of liquid-to-solid conversion for sulfur in T-*h*PC/PP. Moreover, the as-obtained

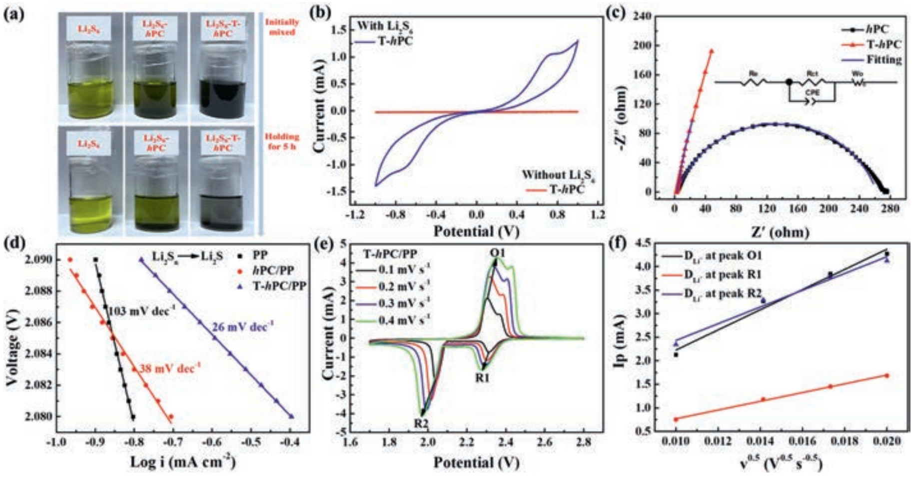

Fig. 5. (a) Photographs of the Li_2S_6 solutions before and after the addition of *h*PC and T-*h*PC powders. (b) CV curves of the *h*PC/PP and T-*h*PC/PP symmetric cells with and without Li_2S_6 electrolyte. (c) EIS spectra of the *h*PC and the T-*h*PC symmetrical cells with Li_2S_6 electrolyte. The inset shows the equivalent circuit model. (d) Tafel plots corresponding to the reductions of Li_2S_n to Li_2S for PP, *h*PC/PP and T-*h*PC/PP. (e) CV curves of the T-*h*PC/PP sample at varied scanning rates and (f) the corresponding plots of reductive and oxidative peak current (I_p) as a function of the square root of the scanning rate ($\upsilon^{1/2}$).

Tafel slope is also quite low among reports for different Li-S interlayers [84].

CV measurements performed at varied scan rates are carried out to further investigate the influences of T-*h*PC interlayer on the electrochemical performance (Figs. 5e and f, Fig. S6 in Supporting information). According to Randles−Sevcik equation [85], the Li^+ diffusion coefficient (D_{Li^+}) can be calculated from the slope of the linear fitting curve between the peak current and the square root of the scan rate. Apparently, the T-*h*PC/PP cell possesses the highest D_{Li^+} among the three cells, at all the recorded redox peaks of O1, R1 and R2, respectively. Also, as summarized in Table S2 (Supporting information), the D_{Li^+} values for cell with the T-*h*PC/PP interlayer are 3.34×10^{-8}, 6.28×10^{-9} and 2.31×10^{-8} cm^2/s, respectively, for the processes of O1, R1, and R2, while for cells with PP (or *h*PC/PP), these values are recorded as 3.36×10^{-8} (or 4.48×10^{-9}), 3.45×10^{-9} (or 2.18×10^{-9}) and 6.46×10^{-9} (or 2.82×10^{-9}) cm^2/s, respectively, indicating a significant increase in the Li^+ mobility kinetics after the addition of the T-*h*PC/PP interlayer. Also, as shown in Fig. S7 (Supporting information), the T-*h*PC/PP also exhibits the smallest polar potential (difference between the anode peak and the cathode peak), indicating a relatively small energy loss during cycling compared with the PP and *h*PC/PP separators.

To investigate the influence of these membranes on the electrochemical performance, asymmetric Li-S batteries are assembled by using PP, *h*PC/PP and T-*h*PC/PP as the separators, and S and Li foil are used as the cathode and the anode, to form a series of CR2032 coin cells. Fig. 6a shows the corresponding CV profiles of the PP, *h*PC/PP and T-*h*PC/PP cells in the range of 1.7–2.8 V at a scan rate of 0.1 mV/s. During the cathodic scanning, the two representative cathodic peaks locating at 2.31 V and 2.04 V can be observed, which are ascribed to the transformation of S_8 to the soluble long-chain lithium polysulfides (Li_2S_x, $4 \leq x \leq 8$) and subsequent transformation to the insoluble short-chain Li_2S_2/Li_2S, respectively [83]. During the anodic scanning, the two recorded anodic peaks are attributed to the conversion of Li_2S_2/Li_2S to polysulfides and then to sulfur [86]. Compared with the Li-S cells with either PP or *h*PC/PP separators, the cell with T-*h*PC/PP separator possesses a larger peak current density and smaller potential gap, which indicates an improved redox kinetics during cycling [34]. This is also evidenced by the electrochemical impedance spectroscopy (EIS) measurements shown in Fig. S7, where the semicircle in the Nyquist plot of T-*h*PC/PP is smaller than that of the *h*PC/PP and PP, respectively, suggesting the lowest charge transfer resistance in T-*h*PC/PP [87]. The rate performances are further tested for these cells at different current rates ranging from 0.05 C to 2 C (Fig. 6b). For the PP cell, the specific capacity decreases rapidly when the current is higher than 1 C, while the *h*PC/PP cell can still deliver specific capacities of 1271.7, 875.1, 732.9, 616.7, 526.2 and 518.7 mAh/g at current densities of 0.05, 0.1, 0.2, 0.5, 1 and 2 C, respectively. In contrast, at a current rate of 0.05 C, the initial discharge specific capacity for the T-*h*PC/PP cell reaches as high as 1551.1 mAh/g, corresponding to 92.6% of the theoretical specific capacity for sulfur (1675.0 mAh/g). When the discharge rate increases from 0.1 C, 0.2 C, 0.5 C and 1 C, to 2 C, the capacities can still maintain 1230.5, 1007.6, 914.2, 746.7 and 634.9 mAh/g, respectively. When the applied current density is switched back to 0.1 C, the specific discharge capacity for the T-*h*PC/PP cell still recovers to 1041.8 mAh/g. Cells with S content as high as 80 wt%, corresponding to an areal loading content of 3.5 mg/cm^2, are also assembled to investigate the effectiveness for the T-*h*PC/PP interlayers (Fig. 6d). An initial specific capacity of 891.8 mAh/g and a cycled specific capacity of 716.3 mAh/g is found after 100 cycles, with a Coulombic efficiency as high as 99.3%, indicating the benefits of high sulfur utilization and excellent cycling stability for the T-*h*PC interlayer.

Fig. 6c presents the long-term GCD test measured at 0.5 C. It can be seen clearly that, after 200 cycles, the T-*h*PC/PP cell can endow a high specific discharge capacity of 893.8 mAh/g (capacity retention rate of 85.5%), corresponding to a capacity decay rate of only 0.04% per cycle. This value is quite low among reports for Li-S interlayers, and comparable to cells using expensive MOFs or complex stacking structures by incorporating heterogeneous catalysis and heterojunction (Table S3 in Supporting information). On the contrary, the routine PP reveals a much lower cycled discharge capacity of 345.3 mAh/g, corresponding to a high capacity decay rate of 0.15% per cycle after 200 cycles. These results highlight the promising benefits of sulfur utilization and polysulfides stabilization from the T-*h*PC/PP interlayers, which are of particular interests for emerging high-performance Li-S batteries.

To further investigate the catalytic functions of TiO_2 in the Li-S battery, XPS measurement for the disassembled cell discharged after 200 cycles at 0.5 C are implemented (Fig. 7). From the high-resolution Ti 2p XPS spectrum in Fig. 7a, typical peak for Ti–S binding can be observed at 454.6 eV, which can be ascribed to the Lewis acid-base interactions formed between unoccupied orbitals of surface Ti atoms and the electronegative polysulfides [34].

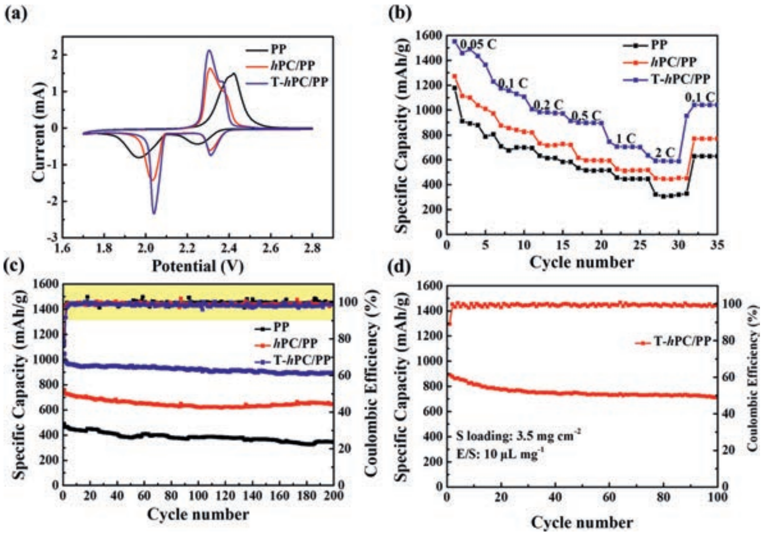

Fig. 6. Electrochemical performance for the PP, *h*PC/PP and T-*h*PC/PP cells. (a) CV curves in a voltage range of 1.7-2.8 V with scanning rate of 0.1 mV/s. (b) Rate performance at various current densities. (c) Long-term cycling stabilities at a current density of 0.5 C. (d) Cycling performance of the CNTs@S cathode with sulfur loading of 3.5 mg/cm^2 at 0.1 C. The E/S ratio is about 10 for this cell.

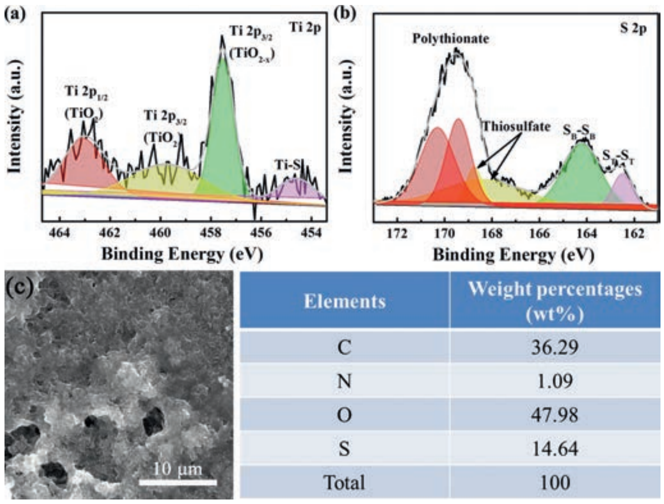

Elements	Weight percentages (wt%)
C	36.29
N	1.09
O	47.98
S	14.64
Total	100

Fig. 7. High-resolution (a) Ti 2p and (b) S 2p XPS spectra of the T-*h*PC after 200 cycles at 0.5 C. SEM images and EDS of (c) T-*h*PC/PP-based cathodes after 200 cycles at 0.5 C.

In the high-resolution S 2p XPS spectrum (Fig. 7b), the T-*h*PC shows several characteristic peaks, corresponding to thiosulfate (168.7/168.3 eV) and polythionate complexes (170.3/169.4 eV), respectively, which are indicative catalytic mediators for the transformation from long-chain to short-chain polysulfides [33,82], showing the benefits of TiO_2 with catalytic effects during the LiPSs conversions.

To better understand the role of the T-*h*PC/PP separator on the suppression of polysulfides shuttling, fully charged Li—S cells after 200 cycles at 0.5 C are disassembled and characterized. As shown in Fig. S9 (Supporting information), no detectable coloration derived from the yellow-colored sulfur or intermediate polysulfides can be found for the T-*h*PC/PP separator along the Li anode side, while for the pristine PP separators, obvious yellow color that indicates the polysulfide migration towards Li anode through the PP separator can be found. Accordingly, as shown in Fig. 7 and Fig. S10 (Supporting information), a great many large unevenly-grown components, ascribed to the sulfur species, can be observed on the cathode surfaces of the PP cell, although, quite smooth and dense morphologies that indicates the relatively uniform coating and growth of the cathode materials during cyclings can be found for *h*PC/PP and T-*h*PC/PP cells. EDS results further demonstrate a higher sulfur conservation content in the cathode of the T-*h*PC/PP cell. These results further imply the successful utilization and stabilization of the active sulfur after incorporation of T-*h*PC interlayers, contributing positive benefits on the cell long-term cycling performances. Attributing to the excellent LiPSs affinity and enhanced catalytic performance from the porous carbon layer supported oxygen-deficient TiO_2 and the low Li^+ ion transport resistance derived from the hierarchical porous carbon, significantly improved electrochemical performance on Li-S batteries are obtained, which enlists the current processing among the most competitive strategies for high-performance Li-S batteries.

In conclusion, we have synthesized a hierarchical porous carbon interlayer embedded with TiO_2-carbon nanocomposites *via* a $T_{i3}C_2$ MXene assisted phase separation and carbonization method. Benefiting from the hierarchical porous structures with a great many micro- to macro-scale multi-pores and the carbon layer supported oxygen deficient $TiO_{2\text{-}x}$ nanoparticles with highly adsorptive and catalytic bifunctionalities, the shuttling of soluble polysulfide intermediates is effectively suppressed along with improved redox reaction kinetics. For Li-S batteries assembled with the T-*h*PC interlayer, an initial discharge specific capacity of 1551.1 mAh/g and a cycled capacity of 893.8 mAh/g after 200 cycles at 0.5 C are obtained, corresponding to a capacity decay rate of only 0.04% per cycle. The strategy demonstrated in this work is quite attractive for building a variety of interesting interlayer for high-performance lithium-sulfur battery.

Declaration of competing interest

The authors declare that they have no known competing financial interests or personal relationships that could have appeared to influence the work reported in this paper.

Acknowledgments

This study was supported in part by funding from the National Natural Science Foundation of China (NSFC, Nos. 51502268, 51325203, 22002142 and 51574205), and the Provincial and Ministerial Co-construction of Collaborative Innovation Center for Resource Materials (No. zycl202008).

Supplementary materials

Supplementary material associated with this article can be found, in the online version, at doi:10.1016/j.cclet.2022.02.034.

References

[1] L.C. Zeng, W.H. Li, Y. Jiang, Y. Yu, Rare Met. 36 (2017) 339–364.
[2] C. Wei, H. Fei, Y. Tian, et al., Chin. Chem. Lett. 31 (2020) 980–983.
[3] R. Kumar, J. Liu, J.Y. Hwang, Y.K. Sun, J. Mater. Chem. A 6 (2018) 11582–11605.
[4] X. Yang, X. Li, K. Adair, H. Zhang, X. Sun, Electrochem. Energy Rev. 1 (2018) 239–293.
[5] S.H. Chung, C.H. Chang, A. Manthiram, Adv. Funct. Mater. 28 (2018) 1801188.
[6] Q. Pang, A. Shyamsunder, B. Narayanan, et al., Nat. Energy 3 (2018) 783–791.
[7] J. Balach, J. Linnemann, T. Jaumann, L. Giebeler, J. Mater. Chem. A 6 (2018) 23127–23168.
[8] X.Q. Zhang, Q. Jin, Y.L. Nan, et al., Angew. Chem. Int. Ed. 60 (2021) 15503–15509.
[9] X. Ji, K.T. Lee, L.F. Nazar, Nat. Mater. 8 (2009) 500–506.
[10] X. Zhao, M. Kim, Y. Liu, et al., Carbon 128 (2018) 138–146.
[11] B. Gan, K. Tang, Y. Chen, et al., J. Energy Chem. 42 (2020) 174–179.
[12] F. Ai, N. Liu, W. Wang, et al., Electrochim. Acta 258 (2017) 80–89.
[13] P. Wang, Z. Zhang, X. Yan, et al., J. Mater. Chem. A 6 (2018) 14178–14187.
[14] X. Zhou, R. Meng, N. Zhong, et al., Small Methods 5 (2021) 2100571.
[15] J. Wu, S. Li, P. Yang, et al., J. Alloys Compd. 783 (2019) 279–285.
[16] D. Cai, B.K. Liu, D.H. Zhu, et al., Adv. Energy Mater. 10 (2020) 1904273.
[17] X. Liang, A. Garsuch, L.F. Nazar, Angew. Chem. Int. Ed. 54 (2015) 3907–3911.
[18] D.S. Wu, F. Shi, G. Zhou, et al., Energy Stor. Mater. 13 (2018) 241–246.
[19] H.J. Peng, J.Q. Huang, X.B. Cheng, Q. Zhang, Adv. Energy Mater. 7 (2017) 1700260.
[20] L. Fan, M. Li, X. Li, et al., Joule 3 (2019) 361–386.
[21] C.L. Lee, I.D. Kim, Nanoscale 7 (2015) 10362–10367.
[22] R. Fang, S. Zhao, S. Pei, et al., ACS Nano 10 (2016) 8676–8682.
[23] F. Pei, L. Lin, A. Fu, et al., Joule 2 (2018) 323–336.
[24] X. Li, Y. Zhang, S. Wang, et al., Nano Lett. 20 (2020) 6922–6929.
[25] S. Zhang, N. Zhong, X. Zhou, et al., Nano-Micro Lett. 12 (2020) 112.
[26] J. Wang, P. Zhai, T. Zhao, et al., Electrochim. Acta 320 (2019) 134558.
[27] M. Zhen, S.Q. Guo, B. Shen, ACS Sustain, Chem. Eng. 8 (2020) 13318–13327.
[28] Z. Zhang, G. Wu, H. Ji, et al., Nanomaterials 10 (2020) 705.
[29] Z. Xiao, Z. Li, X. Meng, R. Wang, J. Mater. Chem. A 7 (2019) 22730–22743.
[30] Y. Dong, S. Zheng, J. Qin, et al., ACS Nano 12 (2018) 2381–2388.
[31] L. Jiao, C. Zhang, C.N. Geng, et al., Adv. Energy Mater. 9 (2019) 1900219.
[32] H. Tang, W.L. Li, L.M. Pan, et al., Adv. Sci. 5 (2018) 1800502.
[33] Z. Xiao, Z. Yang, Z. Li, P. Li, R. Wang, ACS Nano 13 (2019) 3404–3412.
[34] P. Li, H. Lv, Z. Li, et al., Adv. Mater. 33 (2021) 2007803.
[35] X. Wang, Z. Wang, L. Chen, J. Power Sources 242 (2013) 65–69.
[36] X. Zhou, Q. Liao, T. Bai, J. Yang, J. Mater. Sci. 52 (2017) 7719–7732.
[37] L. Ma, K.E. Hendrickson, S. Wei, L.A. Archer, Nano Today 10 (2015) 315–338.
[38] M. Chen, S. Jiang, C. Huang, et al., ChemSusChem 10 (2017) 1803–1812.
[39] K. Gao, D. Xia, H. Ji, et al., Energy Fuels 35 (2021) 10303–10314.
[40] T. Shah, S. Halacheva, Adv. Smart Med. Textiles (2016) 119–154.
[41] X. Li, K. Teng, J. Shi, et al., J. Taiwan Instit. Chem. Engin. 60 (2016) 636–642.
[42] H. Liu, F.Y. Gao, Q.C. Fan, et al., J. Electroanal. Chem. 873 (2020) 114409.
[43] L. Zhang, Y.L. Hsieh, Nanotechnology 17 (2006) 4416–4423.
[44] C. Liu, Y. Tan, Y. Liu, et al., J. Energy Chem. 25 (2016) 587–593.
[45] L. Gao, C. Li, W. Huang, et al., Chem. Mater. 32 (2020) 1703–1747.
[46] Y. Yang, L. Shi, Z. Cao, R. Wang, J. Sun, Adv. Funct. Mater. 29 (2019) 1807882.
[47] T.X. Shang, Z.F. Lin, C.S. Qi, et al., Adv. Funct. Mater. 29 (2019) 1903960.
[48] D. Xiong, X. Li, Z. Bai, S. Lu, Small 14 (2018) 1703419.
[49] A. Lipatov, M. Alhabeb, M.R. Lukatskaya, et al., Adv. Electron. Mater. 2 (2016) 1600255.
[50] Y.Q. Shi, C. Liu, L. Liu, et al., Chem. Eng. J. 378 (2019) 122267.
[51] S. Li, Z. Cui, L. Zhang, B. He, J. Li, J. Membr. Sci. 513 (2016) 1–11.
[52] Z. Wang, F. Yan, H. Pei, et al., Carbohydr. Polym. 198 (2018) 241–248.
[53] Y.T. Liu, P. Zhang, N. Sun, et al., Adv. Mater. 30 (2018) 1707334.
[54] M. Yu, J. Ma, H. Song, et al., Energy Environ. Sci. 9 (2016) 1495–1503.
[55] J. Ren, Y. Zhou, M. Guo, Q. Zheng, D. Lin, Int. J. Hydrog. Energy 43 (2018) 20022–20032.
[56] H. Pan, X. Huang, R. Zhang, et al., Chem. Eng. J. 358 (2019) 1253–1261.
[57] D.C. Xia, J.P. Quan, G.D. Wu, et al., Nanomaterials 9 (2019) 1225.
[58] J. Zhang, C.P. Yang, Y.X. Yin, L.J. Wan, Y.G. Guo, Adv. Mater. 28 (2016) 9539–9544.
[59] F. Chen, J. Yang, T. Bai, B. Long, X. Zhou, Electrochim. Acta 192 (2016) 99–109.
[60] W. Bao, X. Tang, X. Guo, et al., Joule 2 (2018) 778–787.
[61] S. Challagulla, K. Tarafder, R. Ganesan, S. Roy, Sci. Rep. 7 (2017) 8783.
[62] L. Kernazhitsky, V. Shymanovska, T. Gavrilko, et al., Ukr. J. Phys. 59 (2014) 246–253.
[63] Z. Cui, T. Mei, J. Yao, et al., J. Alloys Compd. 753 (2018) 622–629.
[64] P. Zhu, J. Zhu, C. Yan, et al., Adv. Mater. Interfaces 5 (2018) 1701598.
[65] H. Huang, Y. Song, N. Li, et al., Appl. Catal. B 251 (2019) 154–161.
[66] Q. Yin, Z. Cao, Z. Wang, et al., Nanotechnology 32 (2021) 015706.
[67] H. Peng, F. Liu, X. Liu, et al., ACS Catal. 4 (2014) 3797–3805.
[68] L. Li, M. Zhang, X. Zhang, Z. Zhang, J. Power Sources 364 (2017) 234–241.
[69] J. Guo, F. Dong, S. Zhong, et al., Catal. Lett. 148 (2018) 359–373.
[70] H.E. Wang, K. Yin, N. Qin, et al., J. Mater. Chem. A 7 (2019) 10346–10353.
[71] Y. Tian, G. Li, Y. Zhang, et al., Adv. Mater. 32 (2020) 1904876.
[72] P. Huo, P. Zhao, X. Shi, Z. Zhou, B. Liu, J. Mater. Sci. 56 (2021) 2138–2149.
[73] B. Bharti, S. Kumar, H.N. Lee, R. Kumar, Sci. Rep. 6 (2016) 32355.
[74] L. Yang, Y. Peng, Y. Yang, et al., ACS Appl, Nano Mater 2 (2019) 1737–1738.
[75] L.C. Sim, K.H. Leong, S. Ibrahim, P. Saravanan, J. Mater. Chem. A 2 (2014) 5315–5322.
[76] S. Umrao, S. Abraham, F. Theil, et al., RSC Adv. 4 (2014) 59890–59901.
[77] I. Hashemizadeh, D.C.W. Tsang, Y.H. Ng, et al., RSC Adv. 7 (2017) 39098–39108.
[78] S. Zhang, H. Liu, B. Cao, et al., J. Mater. Chem. A 7 (2019) 21766–21773.
[79] F. Miao, C. Shao, X. Li, et al., J. Mater. Chem. A 4 (2016) 5623–5631.
[80] F. Pei, L. Lin, D. Ou, et al., Nat. Commun. 8 (2017) 482.
[81] Y. Jiang, Y. Deng, B. Zhang, et al., Nanoscale 12 (2020) 12308–12316.
[82] H. Zhang, L. Yang, P. Zhang, et al., Adv. Mater. 33 (2021) 2008447.
[83] R. Li, H. Peng, Q. Wu, et al., Angew. Chem. Int. Ed. 59 (2020) 12129–12138.
[84] W. Hua, H. Li, C. Pei, et al., Adv. Mater. 33 (2021) 2101006.
[85] X. Zhang, L.L. Zhu, Z.X. Gao, et al., Mater. Today Commun. 28 (2021) 102666.
[86] G. Jiang, N. Zheng, X. Chen, et al., Chem. Eng. J. 373 (2019) 1309–1318.
[87] X.a. Chen, Z. Xiao, X. Ning, et al., Adv. Energy Mater. 4 (2014) 1301988.